

Black–Bounce via Gravitational–Tension Screening Acting as an Analogue of Schwinger Corrections

Milko Estrada^{1,*}

¹*Departamento de Física, Facultad de Ciencias,
Universidad de Tarapacá, Casilla 7-D, Arica, Chile*

(Dated: June 2, 2026)

Abstract

We provide a novel geometric regularization mechanism for black-bounce spacetimes based on an effective gravitational-tension screening inspired by Schwinger-like saturation effects. The construction assumes that the gravitational tension associated with the vacuum geometry does not grow indefinitely in high-curvature and short scales regimes, but dynamically approaches a finite critical value. As a result, the scale function acquires tension-dependent corrections, giving rise to a regular bounce structure without introducing ad hoc regular cores. The mechanism generates regular geometries with spherical, planar, and hyperbolic transverse sections, describing regular black holes (RBHs), extremal RBHs, and traversable wormholes. A key result is that the bounce location emerges dynamically from the interplay between gravitational tension and geometric screening. Depending on the regime, the bounce may remain associated with short-distance scales or be displaced toward larger finite-scale regions, indicating that saturation effects can modify not only the inner structure of compact objects at short scales but also their global geometry. Hyperbolic and planar RBHs may satisfy the standard energy conditions near the bounce. Moreover, the hyperbolic geometry exhibits distinctive features, including regular negative-mass configurations and a strong dependence of the energy conditions on the system parameters. In contrast, the matter sources supporting wormhole geometries, as expected, violate the energy conditions near the throat.

arXiv:2606.02393v1 [gr-qc] 1 Jun 2026

* milko.estrada@gmail.com

I. INTRODUCTION

In recent years, observations such as the detection of gravitational waves from the merger of rotating black holes [1], together with the images of the centers of the galaxies M87 [2] and Sagittarius A* [3], have shown remarkable agreement with the predictions of General Relativity (GR), providing strong observational evidence for the existence of black holes. These observations have opened the possibility of directly probing the strong-gravity regime and testing different geometric proposals beyond the standard classical scenarios. In this context, a particularly relevant line of research aims to understand to what extent effective modifications of the space-time geometry at short scales could alter the internal structure of black holes without modifying their expected asymptotic behavior.

Despite its phenomenological success, the usual black hole solutions in GR contain physical singularities where curvature invariants diverge and the classical description of spacetime ceases to be valid. From a physical viewpoint, such singularities are associated with the unbounded growth of tidal forces near the origin. In this connection, it is well known that tidal-force effects can be characterized through the Kretschmann invariant [4]. In a vacuum spacetime with constant transverse section, this quantity behaves as $K \sim \bar{M}^2/r^6$, implying that tidal forces diverge at short distances near the origin. Related to this, the gravitational tension may then be associated with the curvature scale defined by the square root of the vacuum Kretschmann scalar, namely $F \sim \sqrt{K_{\text{vacuum}}} \sim \bar{M}/r^3$. Such a relation is physically reasonable, since the spacetime tension is expected to grow with the mass of the gravitational source [5]. This observation suggests that the singularity problem could be intimately related to the absence of mechanisms capable of dynamically saturating the geometry in high-curvature regimes at short scales. Within this framework, regular black holes (RBHs) have been widely studied as effective models designed to avoid the appearance of physical singularities at short or Planckian scales [6]. Numerous realizations have been proposed, including models involving exotic matter and quantum corrections to classical solutions. Among them, the regular Dymnikova model (DyM) [7] is particularly interesting, since it incorporates an energy density of the form $\rho \sim \exp(-F_c/F) \sim \exp(-r^3/a^3)$, where F_c and a represent a critical gravitational tension and a scale parameter, respectively. In this way, the model encodes the gravitational information of the underlying vacuum solution through an exponential geometric screening mechanism, keeping the energy density finite precisely in the region where tidal forces and gravitational tension would diverge in the vacuum case at short scales. It is worth emphasizing that many usual RBH models incorporate potentially unstable de Sitter cores [8],

which motivates the search for alternative mechanisms of geometric regularization.

The physical structure underlying the DyM model has attracted considerable interest due to its formal similarity with the pair-production factor appearing in the Schwinger effect in quantum electrodynamics. Along these lines, Ref. [9] discussed a possible speculative connection between both mechanisms, suggesting that the effects associated with gravitational collapse could be interpreted in terms of effective processes induced by a critical gravitational tension. Subsequently, Ref. [10] considered a gravitationally induced electric field with $E \sim F$, establishing a more direct analogy with the Schwinger mechanism. This idea has been explored in regular black holes and wormholes in Refs. [5, 11], extended to the Pure Lovelock framework in Ref. [12], studied in connection with thermodynamics and quasinormal modes in Ref. [13], and applied to wave propagation in slowly rotating wormholes in Ref. [14]. In a conceptually related manner, although within a different framework, Refs. [15, 16] also connect the Schwinger electric field with the Kretschmann scalar. Altogether, these results suggest that geometric regularization could emerge from effective saturation mechanisms associated with critical gravitational-tension scales.

On the other hand, within the study of nonsingular compact objects, black-bounce spacetimes [17] have attracted considerable attention due to their ability to smoothly interpolate between RBHs and traversable wormholes. In these models, the causal structure does not terminate at a physical singularity, but instead extends toward a future causal region of the universe. Depending on the parameter space, these geometries may describe one-way or two-way traversable wormholes, as well as RBHs, without necessarily requiring potentially unstable de Sitter cores. Various physical aspects of these models have been investigated recently, including gravitational lensing [18], gravitational-wave echoes [19], electromagnetic properties of accretion disks [20], tidal forces [21], and additional recent applications [22–27].

From a more general perspective, there has also been growing interest in the theoretical study of static pseudo-spherically symmetric spacetimes with hyperbolic or planar transverse sections, associated with both wormholes [28, 29] and black holes [30–34]. In particular, black holes with hyperbolic sections exhibit nontrivial causal properties, since they may possess event horizons even for negative values of the mass parameter [35, 36]. There also exist examples with nonconstant transverse sections [37–39], although this scenario lies beyond the scope of the present work.

Motivated by these ideas, in this work we propose an effective mechanism of geometric saturation in high-curvature regimes at short scales, based on a gravitational-tension-dependent geometric screening structure for black-bounce spacetimes. More specifically, we consider effective short-scale

corrections to the extended radial coordinate of the form $l^2 \rightarrow l^2 + \text{Correction}$ at short scales, where the correction depends dynamically on the gravitational tension associated with the corresponding vacuum geometry through a screening factor $\Gamma \sim \exp(-F_c/F)$ analogous to the Schwinger factor. This mechanism naturally induces a saturated short-distance regime, keeping the relevant geometric quantities bounded while simultaneously recovering the usual asymptotic behavior in the weak-field regime. In addition, we investigate this construction in the cases where the transverse section possesses constant spherical, hyperbolic, and planar curvature

II. PHYSICAL AND GEOMETRICAL ANALYSIS

A. Transverse section

We start by describing the line element of a two-dimensional transverse section

$$ds_T^2 = \frac{d\rho^2}{1 - k\rho^2} + \rho^2 d\phi^2, \quad (1)$$

where $k = 1, -1, 0$. As we will see below, k represents the curvature of the surface: $k = 1$ to a spherical geometry (positive curvature), $k = -1$ corresponds to a hyperbolic geometry (negative curvature), and $k = 0$ to a plane geometry.

We perform the following change of variable:

$$\rho = \begin{cases} \sin \theta & \text{for } k = +1 \\ \sinh h & \text{for } k = -1 \\ p & \text{for } k = 0 \end{cases} \quad (2)$$

which leads to the following form for the transverse section:

$$ds_{T-k}^2 = \begin{cases} d\theta^2 + \sin^2 \theta d\phi^2 & \text{for } k = +1 \\ dh^2 + \sinh^2 h d\phi^2 & \text{for } k = -1 \\ dp^2 + p^2 d\phi^2 & \text{for } k = 0 \end{cases} \quad (3)$$

In this way, the transverse section of the last equation represents a sphere \mathcal{S}^2 , a hyperboloid \mathcal{H}^2 , or a plane \mathcal{R}^2 . In the spherical case, the transverse metric is defined with coordinate ranges $0 \leq \theta \leq \pi$ and $0 \leq \phi < 2\pi$. In the hyperbolic case, the transverse metric is defined with coordinate ranges $-\infty < h < \infty$ and $0 \leq \phi < 2\pi$. In the planar case, the transverse metric is defined with coordinate ranges $0 \leq p < \infty$ and $0 \leq \phi < 2\pi$. Thus, the usual two-dimensional transverse spheres

are replaced by two-dimensional transverse pseudo-spheres. As mentioned in the introduction, in general, any static spacetime can be written in a form corresponding to a transverse section of constant curvature spherical, planar, or hyperbolic, describing a non-trivial compact object such as a wormhole or a black hole.

B. The Spacetime

As we will see later, we will study black-bounce-type geometries [17] capable of reproducing black holes, such that the Killing horizon (determined by the condition $g_{00} = 0$) and an outer marginally trapped surface (the causal horizon, determined by the condition $g_{11}^{-1} = 0$) coincide. This is achieved directly (among other possibilities) in the case where $g_{00} = -(g_{11})^{-1}$. Thus, we begin by analyzing the simplest case, given by the following line element

$$ds^2 = -A(R(l)) dt^2 + \frac{dl^2}{A(R(l))} + R(l)^2 \cdot ds_{T-k}^2 \quad (4)$$

where t is a temporal coordinate representing the proper time of a static observer, and l represents the proper distance at fixed t also referred to as the extended-radial coordinate. The function $R(l)$ can be interpreted as a scale function of the transverse section of constant curvature, spherical, hyperbolic, or planar. In agreement with the previous subsection, the coordinates range as follows:

$$\text{For } k = 1: \quad -\infty < t < \infty, \quad -\infty < l < \infty, \quad \theta \in [0, \pi], \quad \phi \in [0, 2\pi] \quad (5)$$

$$\text{For } k = -1: \quad -\infty < t < \infty, \quad -\infty < l < \infty, \quad -\infty < h < \infty, \quad \phi \in [0, 2\pi] \quad (6)$$

$$\text{For } k = 0: \quad -\infty < t < \infty, \quad -\infty < l < \infty, \quad 0 \leq p < \infty, \quad \phi \in [0, 2\pi] \quad (7)$$

C. The generic scale function

We perform the embedding of the metric into a three-dimensional Euclidean spacetime. In this way, we assume a spatial hypersurface at constant t . For this, for simplicity, we use the following assumptions:

$$\text{For } k = 1: \quad \theta = \theta_0 = \pi/2 \quad (8)$$

$$\text{For } k = -1: \quad h = h_0 = \sinh^{-1}(1) \quad (9)$$

$$\text{For } k = 0: \quad p = p_0 = 1 \quad (10)$$

First, we can note that the induced metric of the transverse section, independently of the value and sign of the curvature k , depends only on the coordinate ϕ , such that $ds_{T-k}^2 \rightarrow d\phi^2$. Thus, the induced metric becomes (at $t = \text{const}$):

$$ds^2 = \frac{dl^2}{A(R(l))} + R(l)^2 d\phi^2, \quad (11)$$

Now we embed this geometry into a three-dimensional Euclidean space with cylindrical coordinates (z, r, ϕ) :

$$ds^2 = dz^2 + dr^2 + r^2 d\phi^2. \quad (12)$$

By comparing Eqs. (11) and (12), while keeping the extended radial coordinate constant, we can identify the Euclidean radius as

$$r = R(l) \quad (13)$$

It is straightforward to notice that, for non-constant l , by comparing Eq. (13), together with $dR = \frac{dR}{dl} dl$, to the Euclidean metric, one can integrate the form of the Euclidean cylindrical coordinate $z(l)$. It is worth mentioning that in the usual black-bounce case [17], where $r = R(l) = \sqrt{l^2 + b_0^2}$ with b_0 a constant, and consequently $l = \pm\sqrt{r^2 - b_0^2}$, the domain of the Euclidean radius is $r \in [b_0, \infty)$, whereas the domain of the proper coordinate is $l \in]-\infty, \infty[$, in agreement with Eqs.(5), (6) and (7).

III. ANALOGUE SCHWINGER-LIKE CORRECTION BLACK BOUNCE MODEL

As mentioned in the introduction, the gravitational tension is associated with the square root of the Kretschmann scalar of the vacuum solution,

$$F \sim \sqrt{K_{\text{vacuum}}} \sim \bar{M}/l^3, \quad (14)$$

where this quantity is related to tidal forces and where \bar{M} is related to the mass parameter of the vacuum geometry. In the literature, the analogy between gravitational tension and the short-distance electric field responsible for the Schwinger effect has been widely discussed. In particular, the ratio

$$\Gamma \sim \exp(-F_c/F) \quad (15)$$

has been interpreted as analogous to the particle–antiparticle production rate [5, 9–14]. In this work, we introduce an effective gravitational tension of the form

$$F_{\text{eff}} = F(1 - \Gamma), \quad (16)$$

In this way, in the previous equation we can identify a geometrical screening factor of $1 - \Gamma$ for the gravitational tension F . In the weak-field regime, corresponding to large distances, one recovers the standard behavior $F_{\text{eff}} \approx F \ll F_c$, while, at short scales, in the high-curvature regime the effective tension dynamically approaches the finite limiting value F_c . In this way, F_c defines the characteristic saturation scale. In this way, the effective gravitational tension encodes the tidal information of the vacuum geometry. At short length scales, where the tidal forces associated with the vacuum gravitational tension diverge, the effective gravitational tension instead saturates to a finite value F_c . As we will discuss below, this behavior may be interpreted as a geometric black-bounce-like effect emerging at quantum scales. Evaluating expression (14) and defining $F_c = \frac{\bar{M}}{a^3}$, where a is a constant, the expression for the effective gravitational tension in (16) becomes:

$$F_{\text{eff}} = \frac{\bar{M}}{l^3} (1 - \exp(-l^3/a^3)) \quad (17)$$

where, according to the previous discussion, at short length scales $l \ll a$, and in strong regimes $F \gg F_c$

$$F_{\text{eff}} \approx F_c + \mathcal{O}\left(\frac{F_c}{F}\right) = \frac{\bar{M}}{a^3} + \mathcal{O}\left(\left(\frac{l}{a}\right)^6\right) \quad (18)$$

while, for weak regimes $F \ll F_c$ at large scales $l \gg a$, the effective electric field becomes negligible

$$F_{\text{eff}} \approx F(l \rightarrow \infty) \rightarrow 0. \quad (19)$$

In agreement with the discussion above, within the context of black-bounce geometries, we propose that the matter sources entering the energy–momentum tensor modify the spacetime geometry through the scale function

$$R(l) = \sqrt{l^2 + F_{\text{eff}}}. \quad (20)$$

In this way, a black-bounce-like behavior may emerge at short scales, where the scale function $R(l)$ is corrected at Planckian scales by a quantum saturation function influenced by the effective gravitational tension, while preserving the standard asymptotic behavior at large scales

$$R(l)^2 = \begin{cases} \text{short scales: } l^2 + \text{quantum-like saturation corrections} \sim l^2 + F_c \sim F_c \\ \text{large scales: } l^2 + \text{Negligible corrections} \sim l^2 \end{cases} \quad (21)$$

The fact that an effective gravitational tension can modify the scale function is physically intuitive, since in general relativity geometry and energy are intrinsically related; consequently, any modification of the geometry necessarily implies a modification of the corresponding matter sources.

Although the analogy involving gravitational tension, the ratio Γ , and the Schwinger effect requires a deeper analysis beyond the scope of the present work, some remarks can nevertheless be made. Within the context of this analogy, the corrections to the scale function, relevant at both short and long distances, could be interpreted as arising from the action of an effective electric field that becomes significant in the high-curvature regime while remaining negligible asymptotically. Such a behavior could be viewed as a consequence of pair creation through the Schwinger effect, which induces a backreaction on the electric field itself. Rather than describing this backreaction through a fully coupled dynamical system — a problem lying beyond the scope of the present work — we could adopt a phenomenological approach in which the dominant effect of pair creation is encoded as an effective screening of the electric field. This screening modifies the spacetime geometry through the scale function, and consequently the matter sources. In this way, the effective field dynamically saturates to a finite value at short scales, while its influence progressively vanishes at large distances.

In this work, we investigate the black bounce scenario. As we shall see below, depending on the values of the parameters involved, this framework may lead to a geometry corresponding to a regular black hole. It is well known that energy, defined as a conserved charge associated with a timelike Killing vector, is well posed at the AdS boundary, without requiring the spacetime to be asymptotically flat. In this way, the geometry described by Eq. (4) is such that the function $A(R(l))$ is

$$A(R(l)) = k + \frac{R(l)^2}{L^2} - \frac{2M}{R(l)} \quad (22)$$

Below, we introduce the form for $R(l)$ adopted in this work, which leads to explicit expressions for the components of the energy–momentum tensor.

A. Parameter Space and Geometrical Black Bounce Structure

We study the regions of the parameter space in which the black bounce model leads to a regular black hole (extremal or non-extremal) or to a wormhole. We begin by analyzing the behavior of the scale function $R(l)$, which is identified with the Euclidean radial coordinate r . In this sense, the bounce occurs where the latter reaches its minimum value. As mentioned before, at short scales, namely in the high-curvature regime, the scale function reaches a finite critical value $R \sim \sqrt{F_c} \sim \sqrt{\bar{M}/a^3}$. In Fig. 1, we observe that for small values of the parameter \bar{M} , the minimum of the scale function occurs at $l \sim 0$, indicating that the bounce is associated with short-distance scales. As \bar{M} increases, however, the location of the minimum is progressively displaced toward positive values

of the extended radial coordinate. The corresponding minimum points (l_0, R_0) are $(0, 1.09545)$ for the red curve, $(1.88456, 2.43703)$ for the blue curve, and $(2.22055, 2.86683)$ for the brown curve. This behavior shows that the screening mechanism not only preserves a finite minimum value of the scale function, thereby maintaining geometric regularity at potentially Planckian scales, but can also dynamically shift the bounce away from the origin toward increasingly larger values of l . Consequently, the saturation effect influences both the short-scale regularization and the global geometric structure of the spacetime. Moreover, it can be directly verified that, in all cases, the first derivative of the scale function vanishes at the minimum, $R'(l_0) = 0$, while the second derivative remains positive, $R''(l_0) > 0$, confirming that these points correspond to genuine bounce locations. For the blue and brown curves, the region around $l \sim 0$ behaves as a saddle-like point. This indicates that, regardless of whether a true minimum is present at this location, the scale function attains a finite value with vanishing first derivative at short scales.

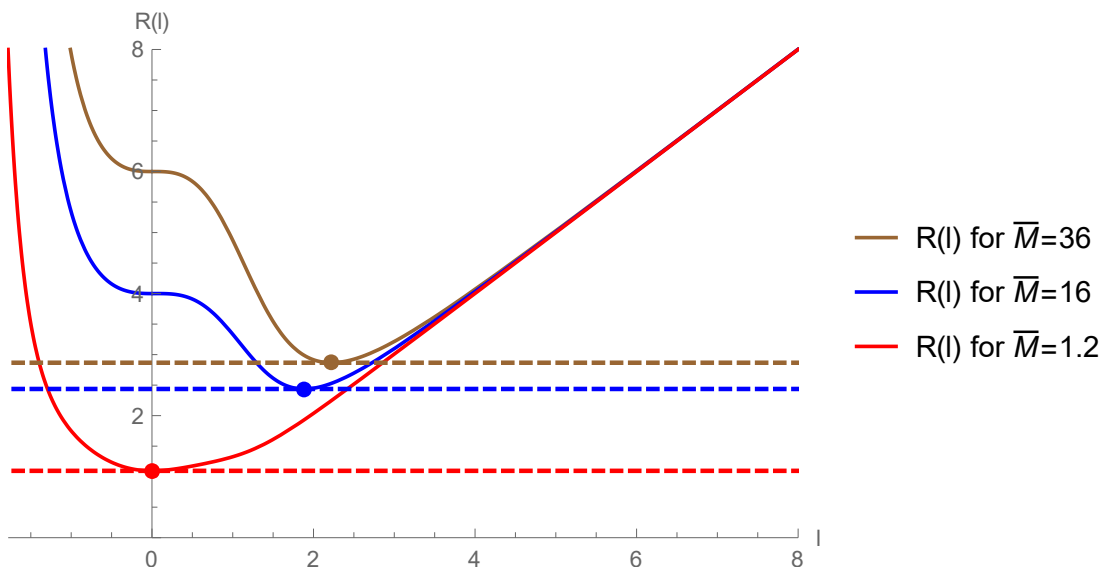


FIG. 1. $R(l)$ for $a = 1$ and $\bar{M} = 36, 16, 1.2$, shown in brown, blue, and red, respectively. The minimum points (l_0, R_0) are given by $(0, 1.09545)$ for the red curve, $(1.88456, 2.43703)$ for the blue curve, and $(2.22055, 2.86683)$ for the brown curve.

We define the mass parameter $M = M_*$ such that the function $A(R(l)) = 0$ at $l = l_*$

$$M_* = M(R(l_*)) = M(R_*) = \frac{k}{2}R_* + \frac{R_*^3}{2L^2}, \quad (23)$$

therefore, every value $l = l_*$ represents the location of a horizon in terms of the extended radial coordinate. On the other hand, as discussed above, the scale function $R(l)$ is identified with the

Euclidean radial coordinate r . Thus, $R(l_*) = R_*$ represents the value at which the scale function, identified with the Euclidean radial coordinate, corresponds to a horizon.

1. Spherically symmetric case, $k = 1$:

In order to analyze the behavior with respect to the extended radial coordinate l , the first and second panels of Fig. 2 display the mass parameter M_* as a function of l_* , and the function $A(l)$ for different values of the parameter M , respectively. Meanwhile, in order to analyze the behavior as a function of the scale function R —which can be identified with the Euclidean radial coordinate r —Fig. 3 displays the mass parameter M_* and the function $A(R)$ in the first and second panels, respectively. We can point out the following:

- In the first panel of Fig. 2 we define $M_*^{(\text{cri})}$ as the minimum value of the mass parameter M_* , associated with the ordered pair $(l_*^{(\text{cri})}, M_*^{(\text{cri})})$. In this way, we observe that for $M = M_*^{(\text{cri})}$ there exists an extremal RBH whose event horizon is located at $l = l_*^{(\text{cri})}$, which coincides with the point where the bounce occurs in Fig. 1, namely l_0 . For the parameter values considered in this figure, the ordered pair associated with the minimum is given by $(l_*^{(\text{cri})}, M_*^{(\text{cri})}) = (2.22055, 13.2142)$. We can verify that the bounce, where the minimum of the scale function $R(l) = R(l_0)$ is attained along the brown curve in Fig. 1, satisfies $l_0 = l_*^{(\text{cri})}$. It is straightforward to verify that this behavior is generic for other values of the parameters. In the second panel of Fig. 2, the brown curve shows that for $M = M_*^{(\text{cri})}$ both horizons coincide, representing an extremal RBH.

This situation can also be visualized in Fig. 3. In the first panel, we observe that for $M = M_*^{(\text{cri})}$ there exists an extremal RBH for which $A(R) = 0$ at $R = R_0$, where R_0 represents the bounce of the scale function identified with the Euclidean radial coordinate. It is worth mentioning that the bounce takes place at the minimum value of R , which in the figure corresponds to $R_0 = 2.8668$ and $M_*^{(\text{cri})} = 13.2142$. In the second panel, we note that, in this case represented by the brown curve, the metric function vanishes exactly at the bounce, and therefore no change of signature. It is worth noting that we can visualize the value R_0 corresponding to the bounce in the vertical dashed line in both panels of Figure 3.

- In the first panel of Fig. 2, for $M > M_*^{(\text{cri})}$ there exists an RBH with two horizons satisfying $l_*^+ > l_*^-$. In the second panel of Fig. 2, the blue curve shows that for $M > M_*^{(\text{cri})}$ two horizons are present, the largest of which corresponds to the RBH event horizon.

This situation can also be visualized in Fig. 3. It can be observed in the first panel that for $M > M_*^{(\text{cri})}$ an event horizon is present. This horizon encloses the value R_0 , identified with r_0 , where the bounce occurs, indicating that the geometry corresponds to an RBH. It is worth mentioning that the bounce takes place at the minimum value of R , which in the figure corresponds to $R_0 = 2.8668$ and $M_*^{(\text{cri})} = 13.2142$. Moreover, the value R_0 associated with the bounce is indicated by the vertical dashed line shown in both panels of Fig. 3. In the second panel, this scenario is represented by the blue curve, where a change of signature can be observed.

- In the first panel of Fig. 2, for $M < M_*^{(\text{cri})}$ no horizons are present, and the geometry corresponds to a traversable wormhole. In the second panel of this figure, the red curve shows that for $M < M_*^{(\text{cri})}$ no horizons exist.

In the first panel of Fig. 3, for $M < M_*^{(\text{cri})}$ no horizons are present. The minimum value of the scale function is given by R_0 , identified with r_0 , implying that no horizon encloses the bounce. This behavior can be visualized in the red curve shown in the second panel. Consequently, the geometry corresponds to a traversable wormhole.

2. Case with constant hyperbolic transverse section, $k = -1$:

As in the spherically symmetric case, the first and second panels of Fig. 4 display the mass parameter M_* as a function of l_* , and the function $A(l)$ for different values of the parameter M , respectively. Similarly, Fig. 5 displays the mass parameter M_* and the function $A(R)$ as functions of the scale function R —identified with the Euclidean radial coordinate r —in the first and second panels, respectively. The brown vertical line in the first and second panels represents the minimum value of the scale function, R_0 , at which the bounce occurs. In the first panel of Fig. 4, we define $M_*^{(\text{cri})}$ as the minimum value of the mass parameter M_* . We also define $M_*^{(\text{cri}1)}$ as a local maximum of M_* , such that $M_*^{(\text{cri})} < M_*^{(\text{cri}1)} < 0$. In this hyperbolic scenario, however, the structure of horizons differs significantly from the spherically symmetric case, as we discuss below:

- We note in the first panel of Fig. 4 that for $M < M_*^{(\text{cri})}$ no horizons are present, and the geometry corresponds to a traversable wormhole admitting negative mass. In the second panel of Fig. 4, this behavior is represented by the blue curve, where the metric function never vanishes.

This situation can also be visualized in Fig. 5. In the first panel, for $M < M_*^{(\text{cri})}$ no horizons are present, implying that no horizon encloses the bounce located at R_0 , identified with r_0 . In the

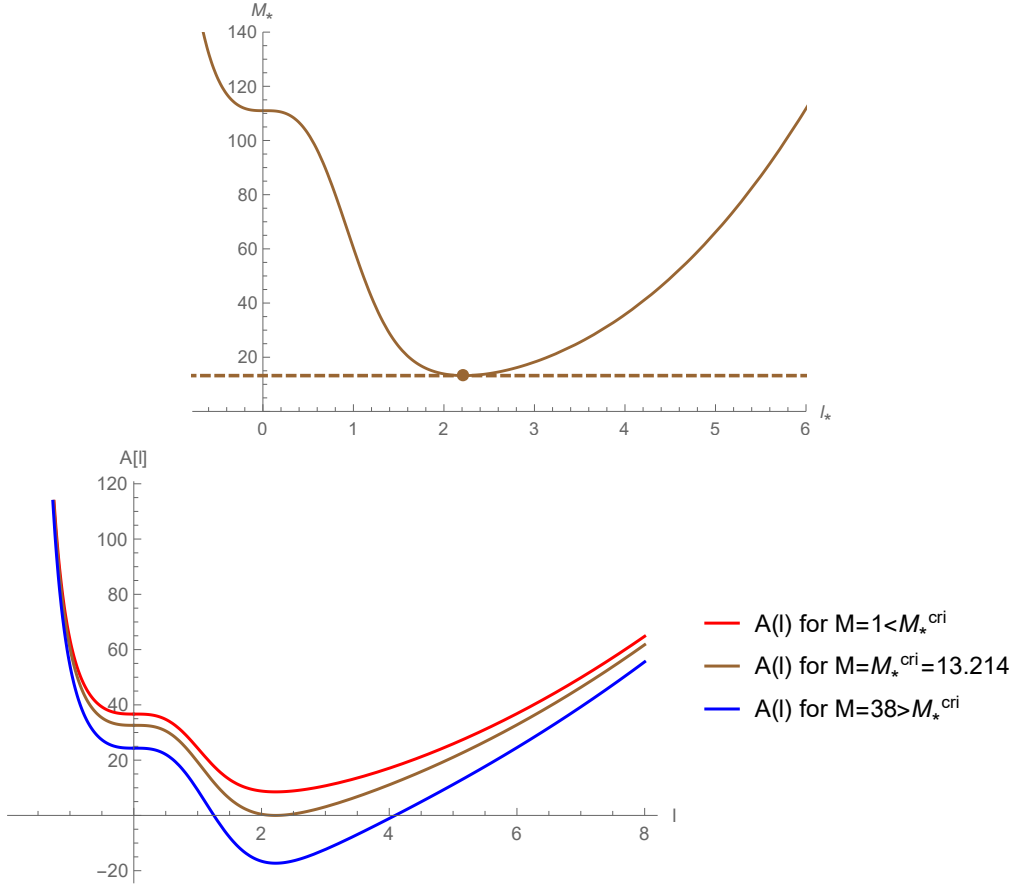


FIG. 2. First panel: The horizontal and vertical axes display l_* and M_* , respectively, such that $A(l_*) = 0$. The minimum point is given by the ordered pair $(l_*^{(\text{cri})}, M_*^{(\text{cri})}) = (2.22055, 13.2142)$. Second panel: The function $A(l)$ is displayed for $M < M_*^{(\text{cri})}$, $M = M_*^{(\text{cri})}$, and $M > M_*^{(\text{cri})}$ in red, brown, and blue, respectively, representing a traversable wormhole, an extremal RBH, and an RBH. The parameter values used are $a = 1$, $\bar{M} = 36$, $L = 1$, $k = 1$.

second panel, represented by the blue curve, the metric function does not vanish. Consequently, the geometry corresponds to a traversable wormhole with negative mass.

- In the first panel of Fig. 4, for $M = M_*^{(\text{cri})}$ there exists an extremal configuration for which two horizons share the same value $M = M_*^{(\text{cri})}$. In the second panel of Fig. 4, this behavior is represented by the brown curve, where the metric function vanishes twice without any change of signature.

This situation can also be visualized in Fig. 5. In the first panel, we observe that for $M = M_*^{(\text{cri})}$ there exists an extremal RBH for which the function $A(R)$ vanishes at a single value, enclosing the bounce located at $R = R_0$. In the second panel, represented by the brown curve, the metric

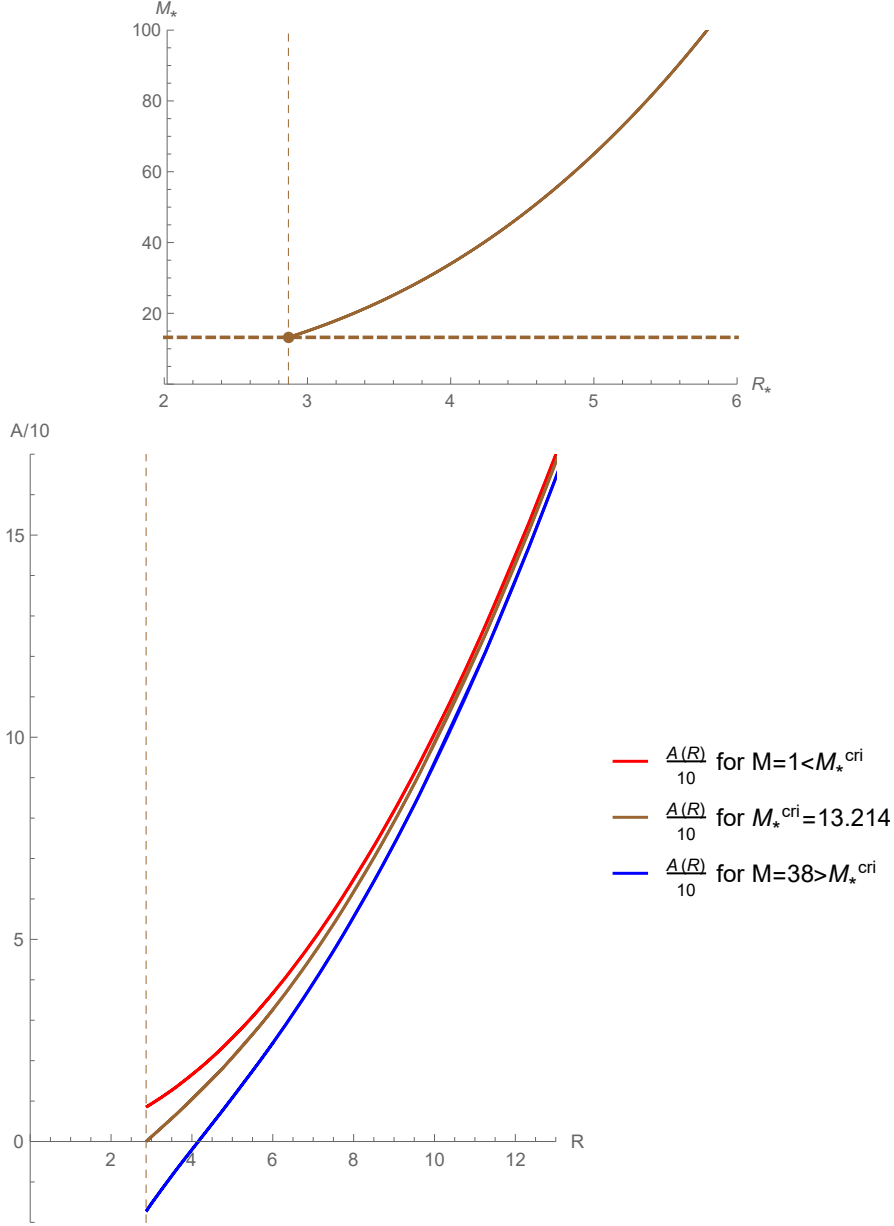


FIG. 3. First panel: The horizontal and vertical axes display R_* and M_* , respectively, such that $A(R_*) = 0$. The minimum point is given by the ordered pair $(R_*^{(\text{cri})}, M_*^{(\text{cri})}) = (2.8668, 13.2142)$. Second panel: The function $A(R)$ is displayed for $M < M_*^{(\text{cri})}$, $M = M_*^{(\text{cri})}$, and $M > M_*^{(\text{cri})}$ in red, brown, and blue, respectively, representing a traversable wormhole, an extremal RBH, and an RBH. $a = 1, \bar{M} = 36, L = 1, k = 1$. The horizon associated with the blue curve is located at $R = R_h = 4.1571$.

function touches the horizontal axis once without any change of signature, corresponding to an extremal RBH configuration.

- In the first panel of Fig. 4, for $M_*^{(\text{cri})} < M < M_*^{(\text{cri}1)}$ there exist four horizons with respect to the

extended radial coordinate l . Therefore, the geometry corresponds to an RBH configuration. In the second panel of Fig. 4, this behavior is represented by the red curve, where four zeros of the metric function are present.

This situation can also be visualized in Fig. 5. In the first panel, for $M_*^{(\text{cri})} < M < M_*^{(\text{cri1})}$ there exist two horizons located at R_+ and R_- , where R_+ corresponds to the event horizon and R_- to the inner horizon. Both the event and inner horizons enclose the bounce located at R_0 , indicating that the geometry corresponds to an RBH. In the second panel, represented by the red curve, a change of signature takes place between both horizons. It is worth mentioning that this RBH configuration admits negative mass.

- In the first panel of Fig. 4, for $M_* = M_*^{(\text{cri1})}$ there exist three horizons with respect to the extended radial coordinate l , where the second one corresponds to a local maximum. Therefore, the geometry corresponds to an RBH configuration. In the second panel of Fig. 4, this behavior is represented by the lower brown curve, where three zeros of the metric function are present.

This situation can also be visualized in Fig. 5. In the first panel, for $M_* = M_*^{(\text{cri1})}$ there exist two horizons located at R_+ and R_- , where R_+ corresponds to the event horizon and R_- to the inner horizon. The inner horizon coincides with the location of the bounce. Both the event and inner horizons enclose the bounce located at R_0 , indicating that the geometry corresponds to an RBH. In the second panel, represented by the lower brown curve, a change of signature takes place between both horizons. It can also be observed that the inner horizon coincides with the location of the bounce. It is worth mentioning that this RBH configuration admits negative mass.

- In the first panel of Fig. 4, for $M > M_*^{(\text{cri1})}$ there exist two horizons with respect to the extended radial coordinate l , corresponding to an RBH geometry. This behavior occurs for both negative and positive values of the mass parameter M . In the second panel of Fig. 4, this situation is represented by the green and purple curves, where two zeros of the metric function are present.

This behavior can also be visualized in Fig. 5. In the first panel, for $M > M_*^{(\text{cri1})}$ the geometry possesses a single event horizon located at R_+ , which encloses the bounce at R_0 . Therefore, the geometry corresponds to an RBH for both negative and positive mass configurations. In the second panel, represented by the green and purple curves, the metric function vanishes at a single value of R , corresponding to the event horizon.

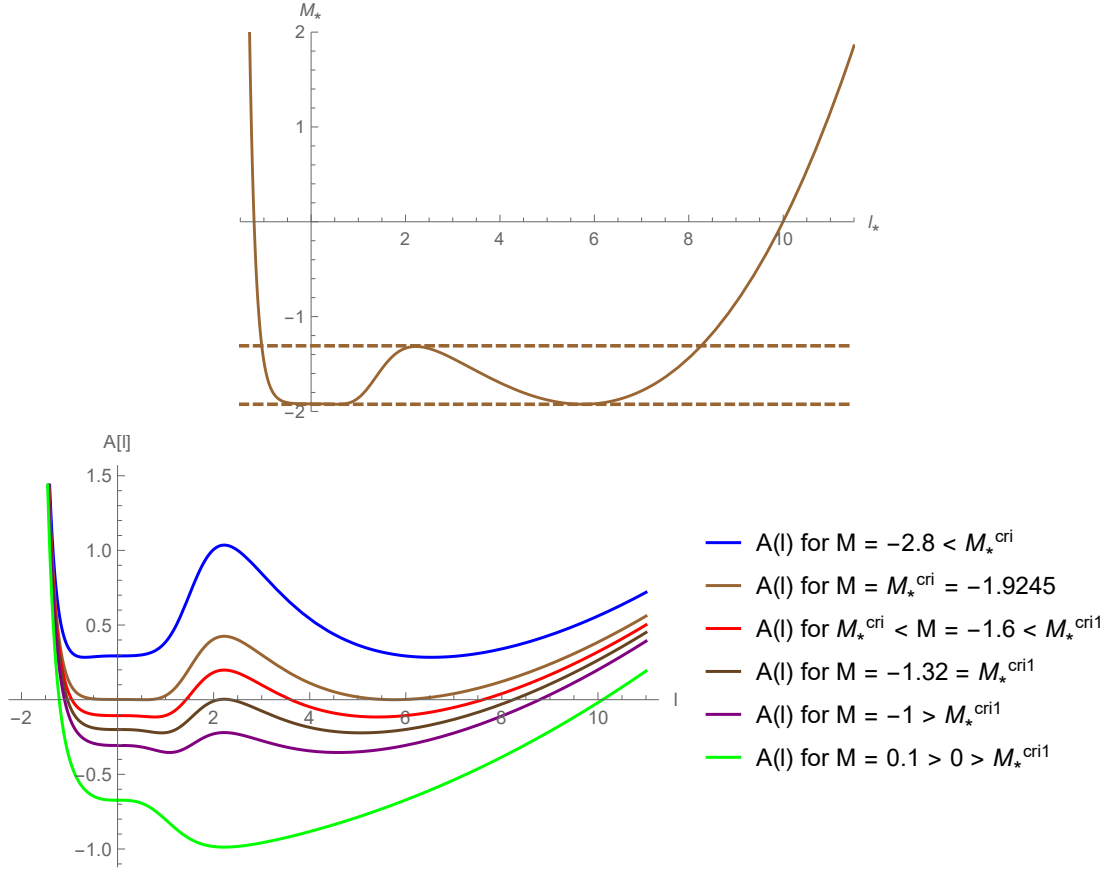


FIG. 4. First panel: Mass parameter M_* as a function of l_* for $a = 1$, $\bar{M} = 36$, $L = 10$, and $k = -1$. Second panel: Function $A(l)$ for $M = -2.8 < M_*^{(\text{cri})}$, $M = M_*^{(\text{cri})} = -1.9245$, $M_*^{(\text{cri})} < M = -1.6 < M_*^{(\text{cri}1)} = -1.32$, $M = M_*^{(\text{cri}1)}$, $M = -1 > M_*^{(\text{cri}1)} < 0$, and $M = 0.1 > 0 > M_*^{(\text{cri}1)}$ with blue, brown, red, brown, purple, and green colors, respectively.

3. Case with constant planar transverse section, $k = 0$:

In order to analyze the behavior with respect to the extended radial coordinate l , the first and second panels of Fig. 6 display the mass parameter M_* as a function of l_* , and the function $A(l)$ for different values of the parameter M , respectively. Meanwhile, in order to analyze the behavior as a function of the scale function R —which can be identified with the Euclidean radial coordinate r —Fig. 7 displays the mass parameter M_* and the function $A(R)$ in the first and second panels, respectively. We can point out the following:

- In the first panel of Fig. 6 we define $M_*^{(\text{cri})}$ as the minimum value of the mass parameter M_* , associated with the ordered pair $(l_*^{(\text{cri})}, M_*^{(\text{cri})})$. In this way, we observe that for $M = M_*^{(\text{cri})}$ there exists an extremal RBH whose event horizon is located at $l = l_*^{(\text{cri})}$, which coincides with the point

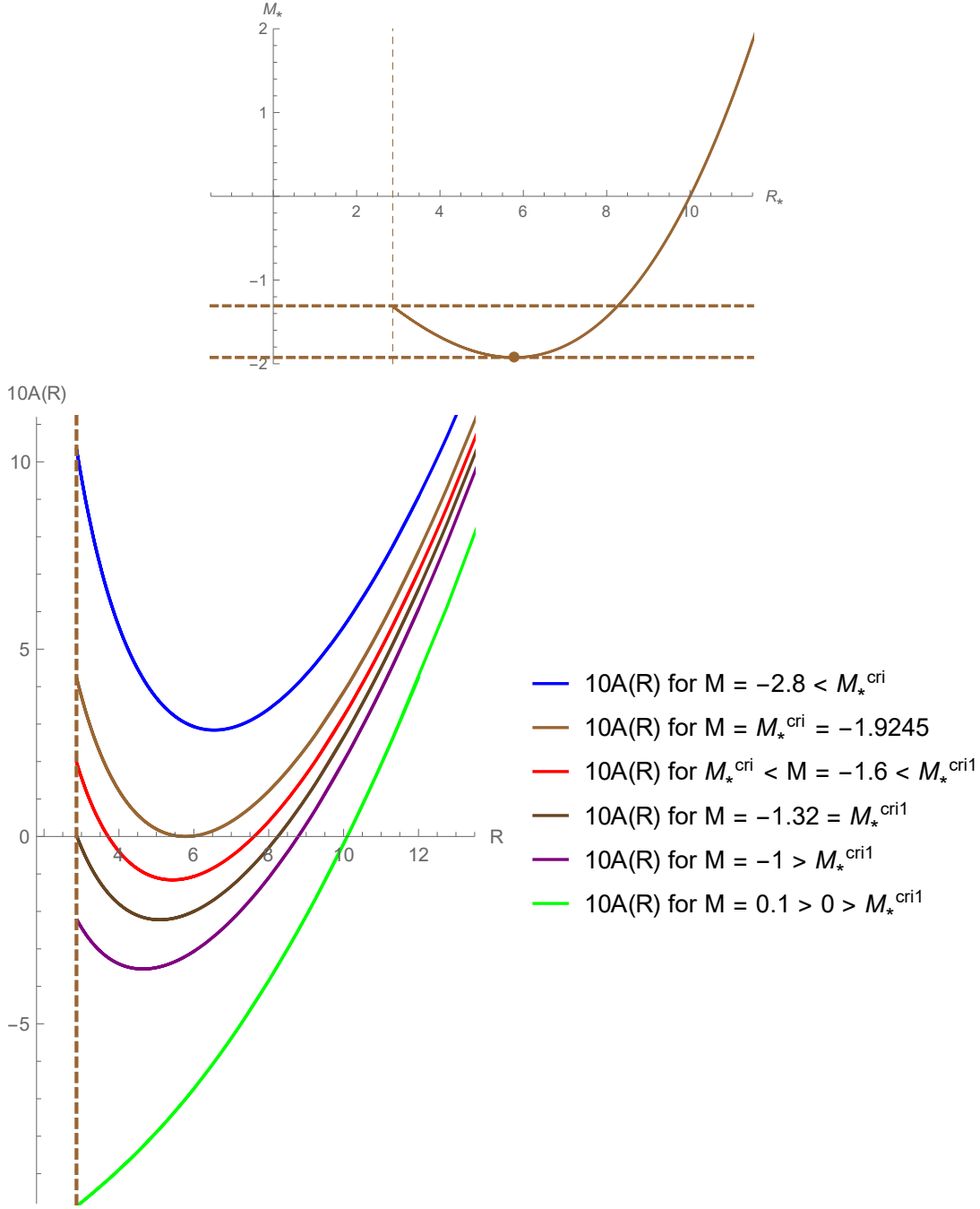


FIG. 5. First panel: Mass parameter M_* as a function of R_* for $a = 1$, $\bar{M} = 36$, $L = 10$, and $k = -1$. Second panel: Function $10 \cdot A(R)$ for $M = -2.8 < M_*^{\text{(cri)}}$, $M = M_*^{\text{(cri)}} = -1.9245$, $M_*^{\text{(cri)}} < M = -1.6 < M_*^{\text{(cri}1)} = -1.32$, $M = M_*^{\text{(cri}1)}$, $M = -1 > M_*^{\text{(cri}1)} < 0$, and $M = 0.1 > M_*^{\text{(cri}1)} > 0$ with blue, brown, red, brown, purple, and green colors, respectively.

where the bounce occurs in Fig. 1, namely l_0 . For the parameter values considered in this figure, the ordered pair associated with the minimum is given by $(l_*^{\text{(cri)}}, M_*^{\text{(cri)}}) = (2.22055, 11.7808)$. We

can verify that the bounce, where the minimum of the scale function $R(l) = R(l_0)$ is attained along the brown curve in Fig. 1, satisfies $l_0 = l_*^{(\text{cri})}$. It is straightforward to verify that this behavior is generic for other values of the parameters. In the second panel of Fig. 6, the brown curve shows that for $M = M_*^{(\text{cri})}$ both horizons coincide, representing an extremal RBH.

This situation can also be visualized in Fig. 7. In the first panel, we observe that for $M = M_*^{(\text{cri})}$ there exists an extremal RBH for which $A(R) = 0$ at $R = R_0$, where R_0 represents the bounce of the scale function identified with the Euclidean radial coordinate. It is worth mentioning that the bounce takes place at the minimum value of R , which in the figure corresponds to $R_0 = 2.8668$ and $M_*^{(\text{cri})} = 11.7808$. In the second panel, we note that, in this case represented by the brown curve, the metric function vanishes exactly at the bounce, and therefore no change of signature occurs. It is worth noting that we can visualize the value R_0 corresponding to the bounce in the vertical dashed line in both panels of Fig. 7.

- In the first panel of Fig. 6, for $M > M_*^{(\text{cri})}$ there exists an RBH with two horizons satisfying $l_*^+ > l_*^-$. In the second panel of Fig. 6, the blue curve shows that for $M > M_*^{(\text{cri})}$ two horizons are present, the largest of which corresponds to the RBH event horizon.

This situation can also be visualized in Fig. 7. It can be observed in the first panel that for $M > M_*^{(\text{cri})}$ an event horizon is present. This horizon encloses the value R_0 , identified with r_0 , where the bounce occurs, indicating that the geometry corresponds to an RBH. It is worth mentioning that the bounce takes place at the minimum value of R , which in the figure corresponds to $R_0 = 2.8668$ and $M_*^{(\text{cri})} = 11.7808$. Moreover, the value R_0 associated with the bounce is indicated by the vertical dashed line shown in both panels of Fig. 7. In the second panel, this scenario is represented by the blue curve, where a change of signature can be observed.

- In the first panel of Fig. 6, for $M < M_*^{(\text{cri})}$ no horizons are present, and the geometry corresponds to a traversable wormhole. In the second panel of this figure, the red curve shows that for $M < M_*^{(\text{cri})}$ no horizons exist.

In the first panel of Fig. 7, for $M < M_*^{(\text{cri})}$ no horizons are present. The minimum value of the scale function is given by R_0 , identified with r_0 , implying that no horizon encloses the bounce. This behavior can be visualized in the red curve shown in the second panel. Consequently, the geometry corresponds to a traversable wormhole.

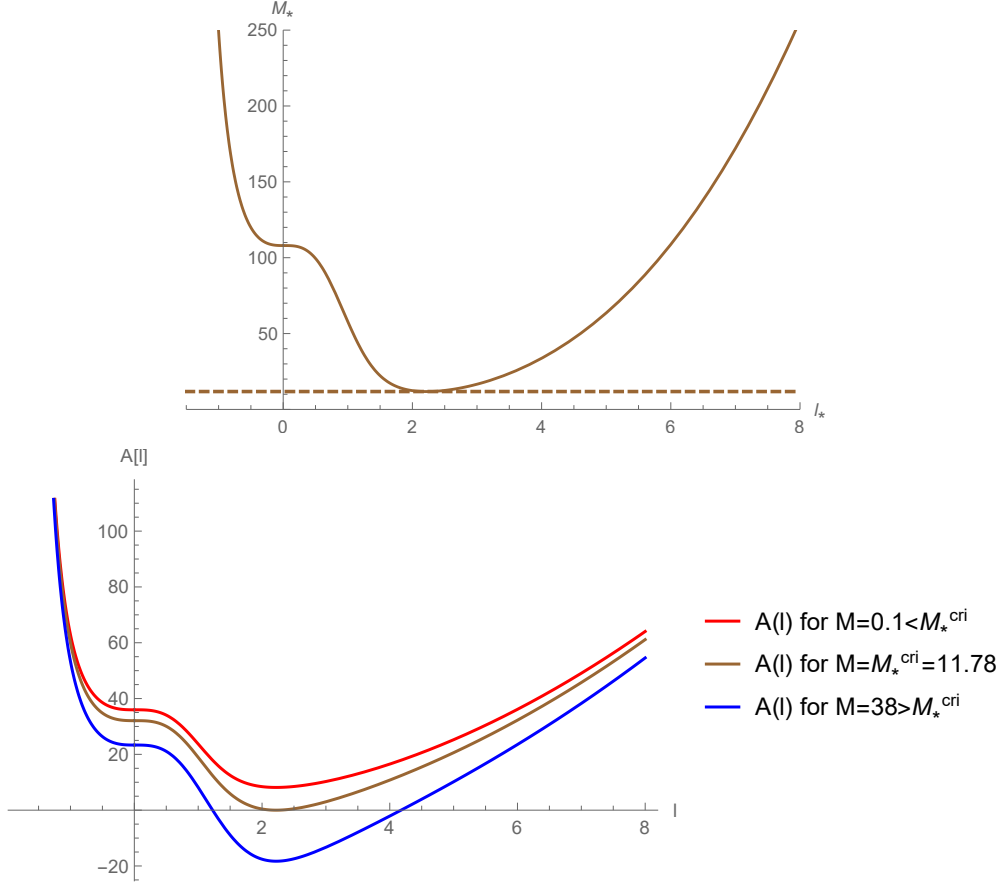


FIG. 6. First panel: The horizontal and vertical axes display l_* and M_* , respectively, such that $A(l_*) = 0$. The minimum point is given by the ordered pair $(l_*^{(\text{cri})}, M_*^{(\text{cri})}) = (2.22055, 11.7808)$. Second panel: The function $A(l)$ is displayed for $M < M_*^{(\text{cri})}$, $M = M_*^{(\text{cri})}$, and $M > M_*^{(\text{cri})}$ in red, brown, and blue, respectively, representing a traversable wormhole, an extremal RBH, and an RBH. The parameter values used are $a = 1$, $\bar{M} = 36$, $L = 1$, $k = 0$.

B. The Kretschmann scalar

It is also worth testing the behavior of the Kretschmann scalar for the three previously discussed cases: spherical, hyperbolic, and planar constant-transverse-section geometries, corresponding to $k = 1$, $k = -1$, and $k = 0$, respectively. The value of the latter for our space-time is given by:

$$K = (A''(l))^2 + 2 \left(\frac{A'(l) R'(l)}{R(l)} \right)^2 + 4 \left(\frac{-k + A(l) R'(l)^2}{R(l)^2} \right)^2 + 2 \left(\frac{A'(l) R'(l) + 2A(l) R''(l)}{R(l)} \right)^2 \quad (24)$$

From the previous analysis, we can observe that in all three cases considered—namely, spherical, hyperbolic, and planar transverse sections—the scale function possesses a nonvanishing minimum,

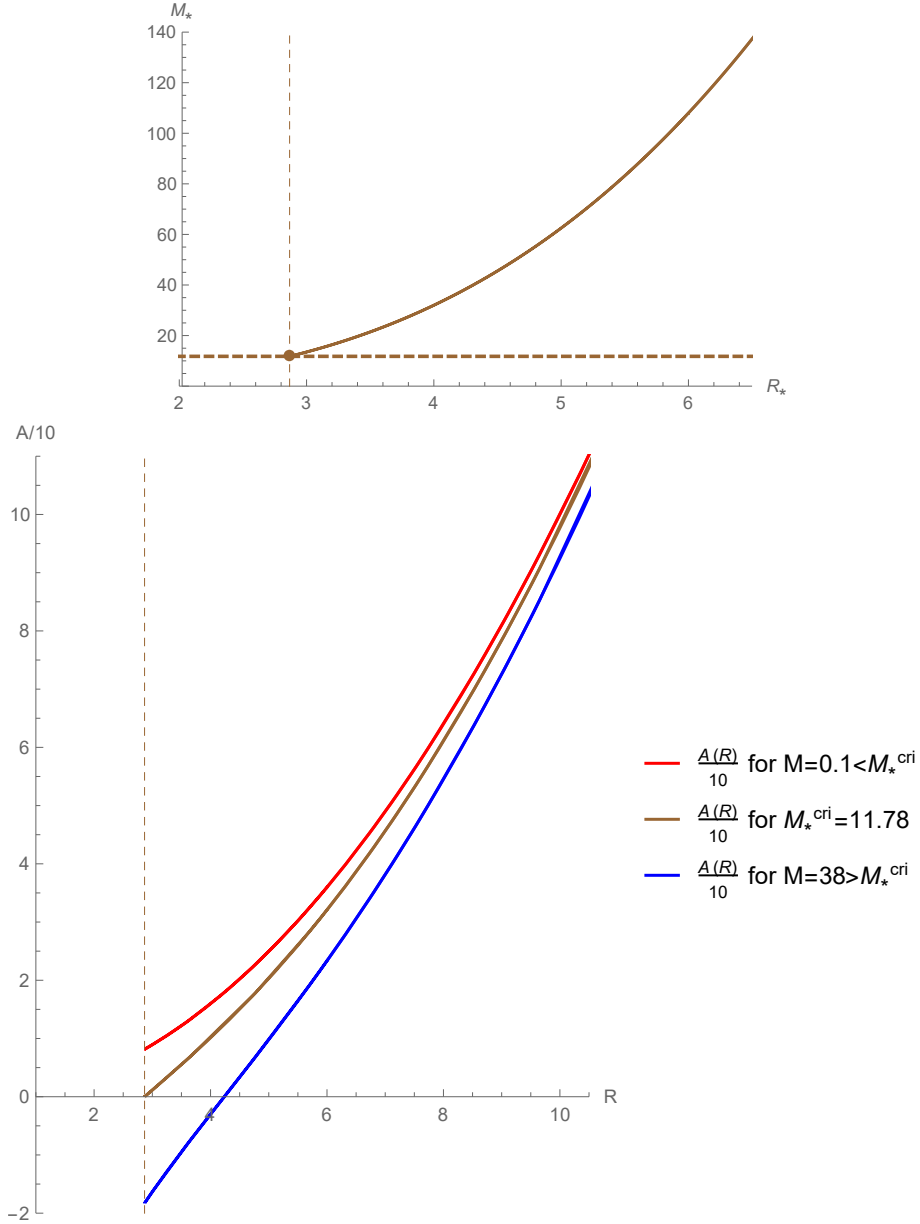


FIG. 7. First panel: The horizontal and vertical axes display R_* and M_* , respectively, such that $A(R_*) = 0$. The minimum point is given by the ordered pair $(R_*^{(\text{cri})}, M_*^{(\text{cri})}) = (2.8668, 11.7808)$. Second panel: The function $A(R)$ is displayed for $M < M_*^{(\text{cri})}$, $M = M_*^{(\text{cri})}$, and $M > M_*^{(\text{cri})}$ in red, brown, and blue, respectively, representing a traversable wormhole, an extremal RBH, and an RBH. The parameter values used are $a = 1, \bar{M} = 36, L = 1, k = 0$. The horizon associated with the blue curve is located at $R = R_h = 4.17711$.

$R(l) > 0$, at which the bounce occurs. Consequently, the Kretschmann scalar does not exhibit divergences associated with the vanishing of this function. Moreover, the graphical analysis indicates that neither the scale function nor $A(l)$, together with their derivatives, develop divergences.

Therefore, the Kretschmann scalar provides information that the geometry remains regular everywhere.

C. Sources and Energy Conditions

We consider the following form for the energy–momentum tensor:

$$T_{\nu}^{\mu} = \text{diag}\left(-\rho(l), p_r(l), p_{\theta}(l), p_{\theta}(l)\right) \quad (25)$$

whose components are

$$\frac{1}{8\pi R(l)^2} \left(-k + A'(l) R'(l) R(l) + A(l) R'(l)^2 + 2A(l) R(l) R''(l) \right) - \frac{3}{8\pi L^2} = -\rho(l) \quad (26)$$

$$\frac{1}{8\pi R(l)^2} \left(-k + A'(l) R'(l) R(l) + A(l) R'(l)^2 \right) - \frac{3}{8\pi L^2} = p_r(l) \quad (27)$$

$$\frac{1}{8\pi R(l)} \left(A'(l) R'(l) + \frac{1}{2}A''(l) R(l) + A(l) R''(l) \right) - \frac{3}{8\pi L^2} = p_{\theta}(l) \quad (28)$$

where $'$ denotes differentiation with respect to the coordinate l and where $k = 1, -1, 0$ when the transverse section in the last equation corresponds, respectively, to a sphere \mathcal{S}^2 , a hyperboloid \mathcal{H}^2 , or a plane \mathcal{R}^2 , described by the transverse line element ds_{T-k}^2 in Eq. (3). The scale function $R(l)$ is given by Eqs. (17) and (20), while the function $A(l)$ is determined by Eq. (22). The conservation equation, through $\nabla_{\mu} T^{\mu\nu} = 0$, is given by:

$$\frac{A'(l)}{2A(l)} \left(\rho(l) + p_r(l) \right) + p_r'(l) + \frac{2R'(l)}{R(l)} \left(p_r(l) - p_{\theta}(l) \right) = 0 \quad (29)$$

where, as is well known, the Bianchi identities imply that the system consists of four equations, of which only three are independent. In this way, the components of the energy–momentum tensor are obtained directly by substituting the corresponding value of k into $A(l)$ and $R(l)$ in Eqs. (26), (27), (28).

For simplicity, we analyze the behavior of ρ , $\rho + p_r$, and $\rho + p_r + 2p_{\theta}$ with respect to the scale function R , which, as discussed above, is identified with the Euclidean radial coordinate r . These quantities are used to test the Weak, Null, and Strong Energy Conditions (WEC, NEC, and SEC), respectively. This procedure allows us to examine these energy conditions more explicitly in the vicinity of the bounce, where R reaches its minimum value. The procedure is repeated for the three cases considered in this work, namely, geometries with spherical, planar, and hyperbolic transverse sections, corresponding to $k = 1$, $k = 0$, and $k = -1$, respectively. In all cases, the parameter values have been chosen in accordance with the analyses presented above.

In Fig. 8, for the spherical case with $k = 1$, the horizontal axis corresponds to the scale function R , while the vertical axis represents ρ , $\rho + p_r$, and $\rho + p_r + 2p_\theta$ in the first, second, and third panels, respectively. The parameters shown in the figure have been chosen in accordance with the analysis carried out in the previous sections. The brown dashed vertical line indicates the location of the bounce, which, in the wormhole case, coincides with the throat. We find that, for both the RBH and the extremal Regular Black hole (eRBH), $\rho > 0$ in the vicinity of the bounce. The blue dashed line marks the location of the event horizon of the RBH at $R = 3$, showing that the WEC is satisfied at the event horizon. In both the RBH and eRBH cases, as R increases, the energy density becomes negative, violating the WEC, and later returns to positive values at finite distances. In contrast, for the wormhole (WH) geometry, $\rho < 0$ near the bounce, which corresponds to the throat, indicating a violation of the WEC in this region, as expected. As R increases further, the energy density becomes positive before turning negative again at larger distances.

The second panel displays the behavior of $\rho + p_r$. Interestingly, for the eRBH, one finds that $\rho = -p_r$ at the location of the bounce, as occurs in the usual spacetimes whose angular sector is given by $r^2 d\Omega^2$. For both the RBH and eRBH, the NEC is satisfied near the bounce, then violated, and finally restored at larger scales. In the wormhole case, the NEC is violated in the vicinity of the throat and again at large distances, as expected. Finally, the third panel tests the SEC through the quantity $\rho + p_r + 2p_\theta$. We find that the SEC is satisfied near the bounce for all three geometries: the RBH, the eRBH, and the wormhole.

An analogous procedure has been followed in the first, second, and third panels of Fig. 9 for the planar case with $k = 0$. We note that, for the parameter values chosen in this figure, the behavior of the energy conditions is analogous to that found in the spherical case.

From Fig. 10, we can verify that, for the hyperbolic case, the behavior of the energy conditions differs from that found in the spherical and planar cases. First, we note that, in the wormhole case, as expected, $\rho < 0$ and $\rho + p_r < 0$ near the throat. Moreover, the DEC is also violated in the vicinity of this location. For the extremal RBH, the aforementioned energy conditions are likewise violated near the bounce. The same behavior is observed for the RBH with negative mass. In contrast, for the positive-mass RBH, all these energy conditions are satisfied in the vicinity of the bounce.

Physically, these results show that the presence of a geometric bounce does not necessarily imply the violation of the energy conditions in its vicinity in the case of regular black holes. In particular, for the spherical and planar cases, the regular black hole geometries satisfy the WEC,

NEC, and SEC near the bounce, suggesting that singularity regularization can be achieved through non-exotic matter sources in this region. In contrast, for wormhole geometries, the violation of the WEC and NEC near the throat remains a generic feature, in agreement with the classical results for traversable wormholes. Moreover, the hyperbolic case exhibits a more intriguing behavior, since the fulfillment of the energy conditions depends sensitively on the value of the mass parameter. In this way, the topology of the transverse section plays an important role in determining the physical nature of the matter sources supporting these regular geometries.

IV. CONCLUSION AND DISCUSSION

In this work, we provide a novel geometric regularization mechanism for black-bounce spacetimes based on an effective gravitational-tension screening inspired by saturation effects analogous to the Schwinger mechanism. The central idea is that the gravitational tension associated with the vacuum geometry does not grow without bound in the high-curvature, short-scale regime, but instead approaches a finite critical value through a dynamical screening factor. This behavior naturally induces corrections to the scale function governing the geometry and leads to the emergence of a regular bounce structure.

A remarkable feature of this construction is that the location of the bounce is not fixed by a constant geometric parameter. Instead, it is determined dynamically by the interplay between the gravitational tension and the screening mechanism. As a consequence, the model predicts two distinct regimes. For moderate values of the screening parameter, the bounce remains associated with short-distance scales, as commonly expected in regular geometries. However, when the screening effects become stronger, the minimum of the scale function, which is identified with the embedded Euclidean radial coordinate, can be shifted toward larger finite values while the geometry remains completely regular. This behavior suggests that geometric saturation may not only regularize the deep interior region of compact objects at short scales, but may also influence the global structure of spacetime in a nontrivial way.

From a geometrical perspective, the proposed framework unifies regular black holes, extremal regular black holes, and traversable wormholes within the same effective construction. The transition between these configurations is controlled by the parameter space of the solution and emerges without modifying the underlying regularization mechanism. This provides a common geometrical origin for different classes of nonsingular compact objects and reinforces the interpretation of black-bounce spacetimes as interpolating geometries connecting regular black holes and wormholes.

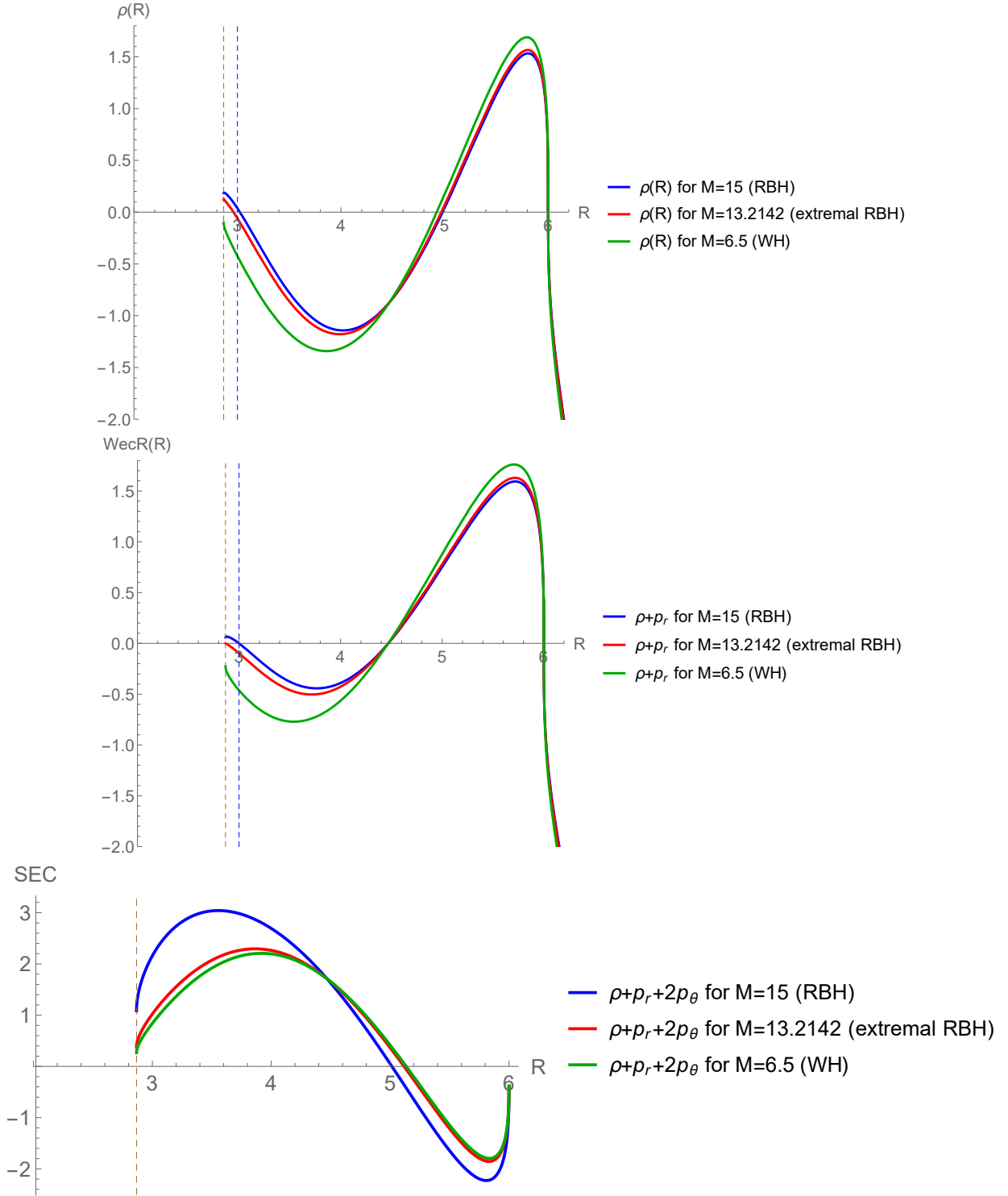


FIG. 8. For $a = 1$, $\bar{M} = 36$, $L = 1$, and $k = 1$, we consider an RBH with $M = 15$, an extremal RBH with $M = 13.2142$, and a WH with $M = 6.5$. The horizontal axis represents R . The vertical axis represents ρ , $\rho + p_r$, and $\rho + p_r + 2p_\theta$ in the first, second, and third panels, respectively. The brown and blue dashed vertical lines indicate the locations of the bounce and the event horizon of the RBH, respectively.

An additional result concerns the role played by the topology of the transverse section. While the spherical and planar cases exhibit qualitatively similar behaviors, the hyperbolic geometry displays a considerably more intriguing structure. In particular, the existence of regular black holes with negative mass and the strong dependence of the energy conditions on the value of the mass parameter indicate that the topology of the transverse section is not merely a mathematical detail, but rather an ingredient that significantly affects the physical properties of the matter sources and the horizon structure.

The analysis of the energy conditions also reveals relevant physical information. Contrary to the common expectation that the existence of a bounce necessarily requires exotic matter, we find that regular black-hole configurations may satisfy the standard energy conditions in the vicinity of the bounce for both spherical and planar topologies. This result suggests that singularity avoidance can be achieved without requiring significant violations of the usual energy conditions precisely in the region where the geometry is regularized. At the same time, wormhole solutions continue to exhibit the expected violations of the energy conditions near the throat, preserving one of the characteristic features of traversable wormholes. Therefore, the present framework allows one to distinguish regular black holes from wormholes through the behavior of the matter sources supporting them.

More generally, the construction presented here introduces a new perspective on geometric regularization. Rather than postulating a regular core from the outset, regularity emerges as a consequence of a saturation mechanism associated with the gravitational tension itself. In this sense, the model establishes a direct connection between high-curvature effects, the saturation of tidal forces, and the formation of nonsingular geometries. This viewpoint may provide an effective phenomenological bridge between classical spacetime descriptions and the modifications expected in regimes where quantum-gravitational effects become relevant. Although such a connection lies beyond the scope of the present work, it opens an interesting question that deserves further investigation.

-
- [1] B. P. Abbott *et al.* (LIGO Scientific, Virgo), “Observation of Gravitational Waves from a Binary Black Hole Merger,” *Phys. Rev. Lett.* **116**, 061102 (2016), arXiv:1602.03837 [gr-qc].
 - [2] Kazunori Akiyama *et al.* (Event Horizon Telescope), “First M87 Event Horizon Telescope Results. I. The Shadow of the Supermassive Black Hole,” *Astrophys. J. Lett.* **875**, L1 (2019), arXiv:1906.11238

[astro-ph.GA].

- [3] Kazunori Akiyama *et al.* (Event Horizon Telescope), “First M87 Event Horizon Telescope Results. VI. The Shadow and Mass of the Central Black Hole,” *Astrophys. J. Lett.* **875**, L6 (2019), arXiv:1906.11243 [astro-ph.GA].
- [4] Iosif Bena, Anthony Houppe, and Nicholas P. Warner, “Delaying the Inevitable: Tidal Disruption in Microstate Geometries,” *JHEP* **02**, 103 (2021), arXiv:2006.13939 [hep-th].
- [5] G. Alencar, Milko Estrada, C. R. Muniz, and Gonzalo J. Olmo, “Dymnikova GUP-corrected black holes,” *JCAP* **11**, 100 (2023), arXiv:2309.03920 [gr-qc].
- [6] Euro Spallucci and Anais Smailagic, “Regular black holes from semi-classical down to Planckian size,” *Int. J. Mod. Phys. D* **26**, 1730013 (2017), arXiv:1701.04592 [hep-th].
- [7] I. Dymnikova, “Vacuum nonsingular black hole,” *Gen. Rel. Grav.* **24**, 235–242 (1992).
- [8] Raúl Carballo-Rubio, Francesco Di Filippo, Stefano Liberati, Costantino Pacilio, and Matt Visser, “Comment on “Regular evaporating black holes with stable cores”,” *Phys. Rev. D* **108**, 128501 (2023), arXiv:2212.07458 [gr-qc].
- [9] I.G. DYMNIKOVA, “De sitter-schwarzschild black hole: Its particlelike core and thermodynamical properties,” *International Journal of Modern Physics D* **05**, 529–540 (1996).
- [10] Stefano Ansoldi, “Spherical black holes with regular center: A Review of existing models including a recent realization with Gaussian sources,” in *Conference on Black Holes and Naked Singularities* (2008) arXiv:0802.0330 [gr-qc].
- [11] Milko Estrada and Celio R. Muniz, “Dymnikova-Schwinger traversable wormholes,” *JCAP* **03**, 055 (2023), arXiv:2301.05037 [gr-qc].
- [12] Milko Estrada and Rodrigo Aros, “Pure Lovelock gravity regular black holes,” *JCAP* **01**, 032 (2025), arXiv:2409.09559 [gr-qc].
- [13] A. Errehymy, Y. Khedif, M. Daoud, K. Myrzakulov, B. Turimov, and T. Myrzakul, “Quantum corrections to Dymnikova-Schwinger black holes in Einstein-Gauss-Bonnet gravity,” *Phys. Lett. B* **870**, 139915 (2025), arXiv:2509.17630 [gr-qc].
- [14] A. Errehymy, Y. Khedif, M. Daoud, B. Turimov, M. A. Khan, and S. Usanov, “Dymnikova-Schwinger quantum-corrected slowly rotating wormholes: Photon and spinning particle dynamics,” (2026), arXiv:2604.03864 [gr-qc].
- [15] Michael F. Wondrak, Walter D. van Suijlekom, and Heino Falcke, “Gravitational Pair Production and Black Hole Evaporation,” *Phys. Rev. Lett.* **130**, 221502 (2023), arXiv:2305.18521 [gr-qc].

- [16] M. N. Chernodub, “On conformal anomaly and pair production,” *Int. J. Mod. Phys. A* **40**, 2540008 (2025), arXiv:2306.03892 [hep-th].
- [17] Alex Simpson and Matt Visser, “Black-bounce to traversable wormhole,” *JCAP* **02**, 042 (2019), arXiv:1812.07114 [gr-qc].
- [18] J. R. Nascimento, A. Yu. Petrov, P. J. Porfírio, and A. R. Soares, “Gravitational lensing in black-bounce spacetimes,” *Phys. Rev. D* **102**, 044021 (2020), arXiv:2005.13096 [gr-qc].
- [19] Yi Yang, Dong Liu, Zhaoyi Xu, Yujia Xing, Shurui Wu, and Zheng-Wen Long, “Echoes of novel black-bounce spacetimes,” *Phys. Rev. D* **104**, 104021 (2021), arXiv:2107.06554 [gr-qc].
- [20] Parth Bambhaniya, Saurabh K. Kimet Jusufi, and Pankaj S. Joshi, “Thin accretion disk in the Simpson-Visser black-bounce and wormhole spacetimes,” *Phys. Rev. D* **105**, 023021 (2022), arXiv:2109.15054 [gr-qc].
- [21] Dhruv Arora, Parth Bambhaniya, Dipanjan Dey, and Pankaj S. Joshi, “Tidal forces in the Simpson–Visser black-bounce and wormhole spacetimes,” *Phys. Dark Univ.* **44**, 101487 (2024), arXiv:2305.08082 [gr-qc].
- [22] Jose R. Nascimento, Ana R. M. Oliveira, Albert Yu. Petrov, Paulo J. Porfírio, and Amilcar R. Queiroz, “Shadow structure of generalized $k - n$ black-bounce metrics,” *Gen. Rel. Grav.* **58**, 26 (2026), arXiv:2510.23748 [gr-qc].
- [23] Yi Ling and Zhangping Yu, “Big bounce and black bounce in quasi-topological gravity,” *JCAP* **03**, 004 (2026), arXiv:2509.00137 [gr-qc].
- [24] Anderson Bragado and Gonzalo J. Olmo, “Periodic equatorial orbits in a black bounce scenario,” *Class. Quant. Grav.* **42**, 185004 (2025), arXiv:2506.15600 [gr-qc].
- [25] Alana C. L. Santos, Leandro A. Lessa, Roberto V. Maluf, and Gonzalo J. Olmo, “Echoes and quasinormal modes of asymmetric black bounces,” (2025), arXiv:2508.11096 [gr-qc].
- [26] L. A. Lessa and G. J. Olmo, “On the structure of black bounces sourced by anisotropic fluids,” *JCAP* **03**, 019 (2025), arXiv:2412.05378 [gr-qc].
- [27] Tiago M. Crispim, Milko Estrada, C. R. Muniz, and G. Alencar, “Braneworld black bounce to traversable wormhole,” *JCAP* **10**, 063 (2024), arXiv:2405.08048 [hep-th].
- [28] Francisco S. N. Lobo and Jose P. Mimoso, “Possibility of hyperbolic tunneling,” *Phys. Rev. D* **82**, 044034 (2010), arXiv:0907.3811 [gr-qc].
- [29] Roberto Avalos, Daniel Brito, Ernesto Fuenmayor, and Ernesto Contreras, “Hyperbolic Casimir-like wormhole,” *Eur. Phys. J. C* **85**, 793 (2025), arXiv:2507.17906 [gr-qc].

- [30] Marco Calzá, Massimiliano Rinaldi, and Sergio Zerbini, “Topological regular black holes without a Cauchy horizon,” *Phys. Rev. D* **112**, 024024 (2025), arXiv:2505.04427 [gr-qc].
- [31] Koichi Nagasaki, “Complexity growth for topological black holes by holographic method,” *Int. J. Mod. Phys. A* **35**, 2050152 (2020), arXiv:1912.03567 [hep-th].
- [32] Jie Ren, “Analytic solutions of neutral hyperbolic black holes with scalar hair,” *Phys. Rev. D* **106**, 086023 (2022), arXiv:1910.06344 [hep-th].
- [33] Hong Guo, Xiao-Mei Kuang, Eleftherios Papantonopoulos, and Bin Wang, “Horizon curvature and spacetime structure influences on black hole scalarization,” *Eur. Phys. J. C* **81**, 842 (2021), arXiv:2012.11844 [gr-qc].
- [34] J. Sadeghi and R. Toorandaz, “Joule-Thomson expansion of hyperscaling violating black holes with spherical and hyperbolic horizons,” *Nucl. Phys. B* **951**, 114902 (2020).
- [35] Robert B. Mann, “Black holes of negative mass,” *Class. Quant. Grav.* **14**, 2927–2930 (1997), arXiv:gr-qc/9705007.
- [36] Robert B. Mann, “Topological black holes: Outside looking in,” *Annals Israel Phys. Soc.* **13**, 311 (1997), arXiv:gr-qc/9709039.
- [37] Jinbo Yang, “Novel topological black holes from thermodynamics and deforming horizons,” *Phys. Rev. D* **109**, 084032 (2024), arXiv:2301.01709 [gr-qc].
- [38] Rodrigo Aros and Milko Estrada, “Study about black hole solutions with nonconstant transversal curvature and its conserved charges in Lovelock gravity,” *Phys. Rev. D* **109**, 104044 (2024), arXiv:2309.04871 [gr-qc].
- [39] Brayden R. Hull and Robert B. Mann, “Thermodynamics of exotic black holes in Lovelock gravity,” *Phys. Rev. D* **104**, 084032 (2021), arXiv:2102.05282 [gr-qc].

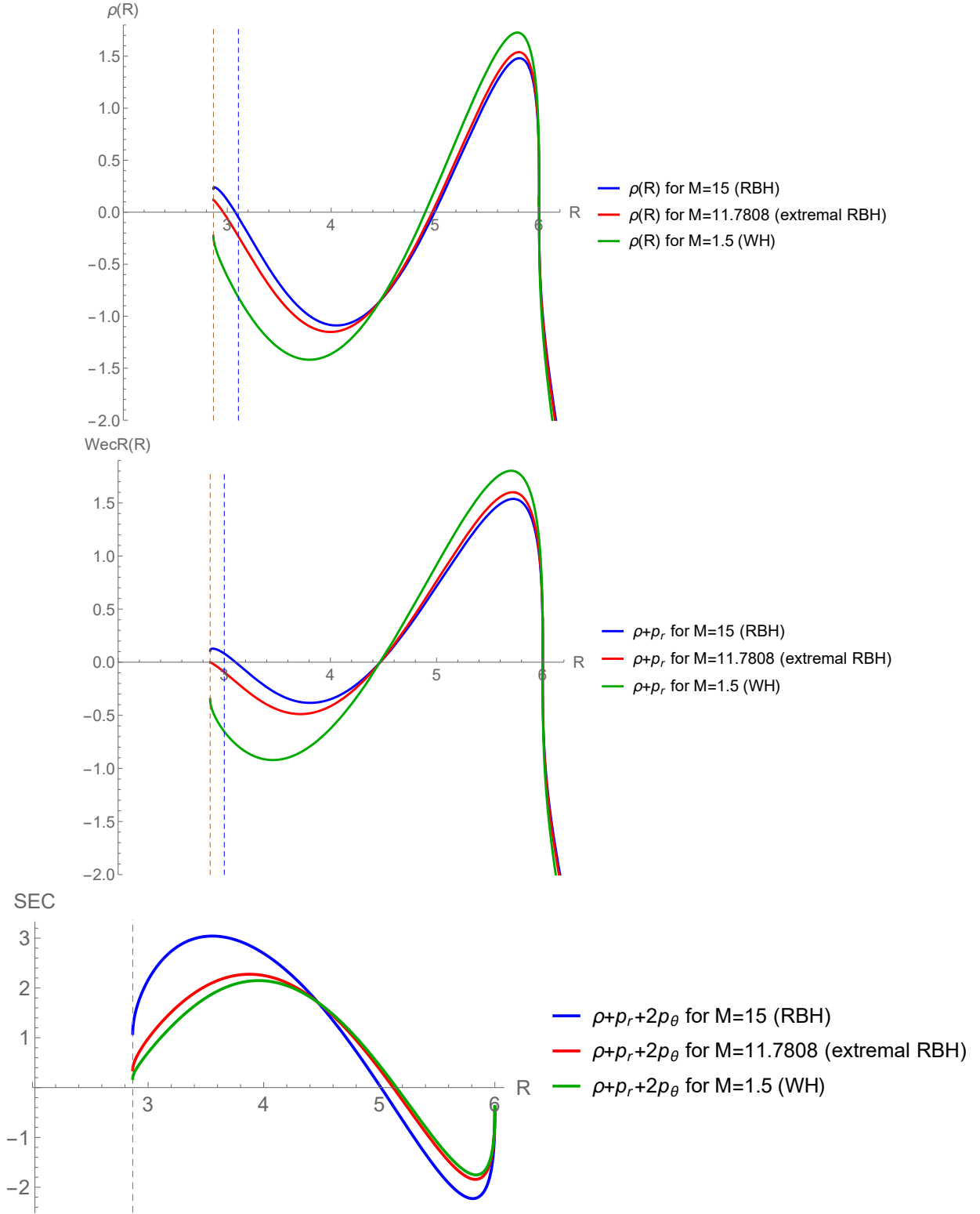


FIG. 9. For $a = 1$, $\bar{M} = 36$, $L = 1$, and $k = 0$, we consider an RBH with $M = 55$, an extremal RBH with $M = 11.7808$, and a WH with $M = 1.5$. The horizontal axis represents R . The vertical axis represents ρ , $\rho + p_r$, and $\rho + p_r + 2p_\theta$ in the first, second, and third panels, respectively. The brown and blue dashed vertical lines indicate the locations of the bounce and the event horizon of the RBH, respectively.

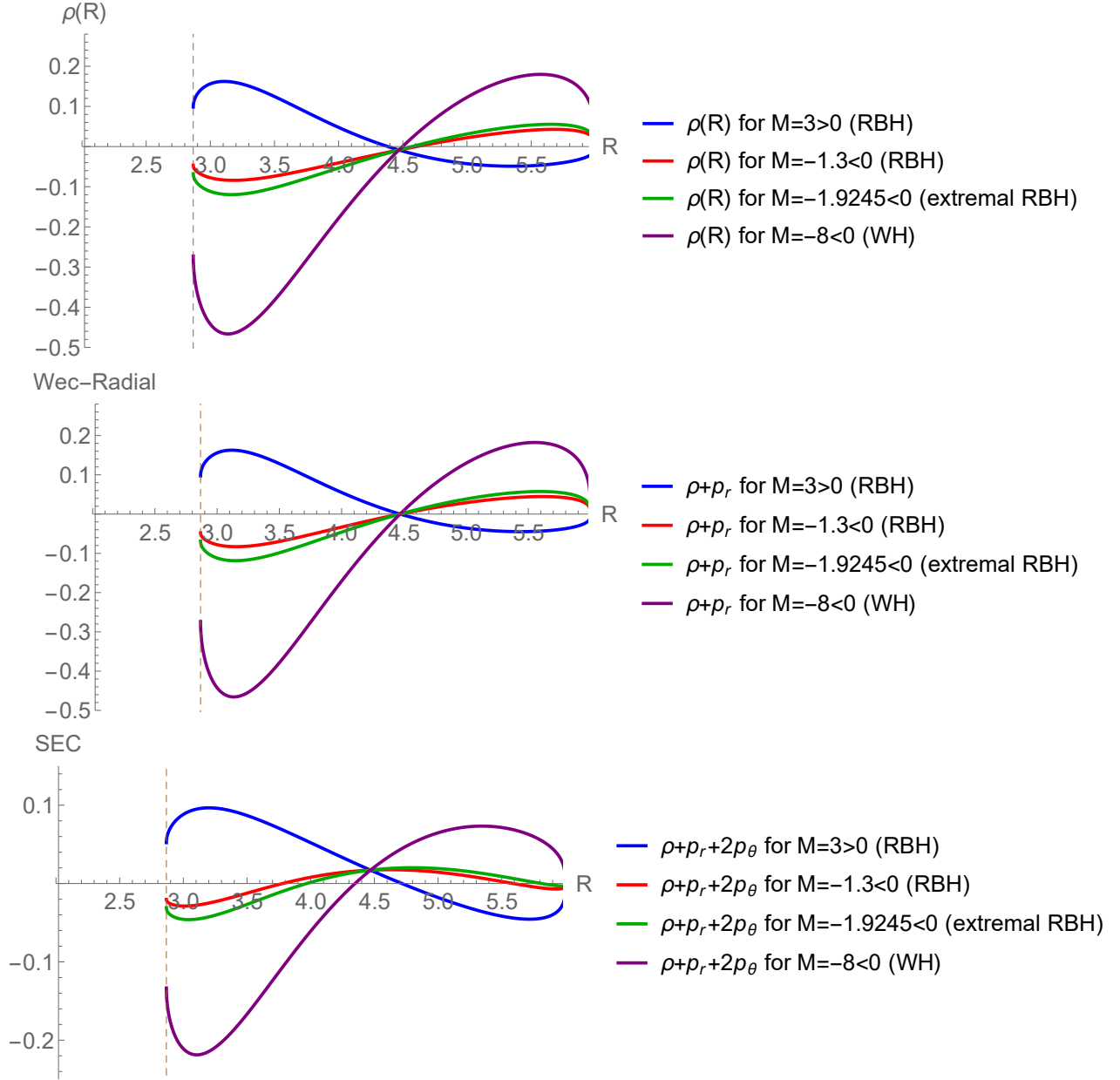


FIG. 10. For $a = 1$, $\bar{M} = 36$, $L = 10$, and $k = -1$, we consider an RBH with $M = 3 > 0$ and $M = -1.3 < 0$, an extremal RBH with $M = -1.9245$, and a WH with $M = -8$. The horizontal axis represents R . The vertical axis represents ρ , $\rho + p_r$, and $\rho + p_r + 2p_\theta$ in the first, second, and third panels, respectively. The brown dashed vertical lines indicate the locations of the bounce.